

Photocurrent quantum yield in suspended carbon nanotube pn junctions

Lee Aspirtarte, Daniel R. McCulley, Ethan D. Minot

Department of Physics, Oregon State University, Corvallis, OR, 97331

We study photocurrent generation in individual suspended carbon nanotube pn junctions using spectrally-resolved scanning photocurrent microscopy. Spatial maps of the photocurrent allow us to determine the length of the pn junction intrinsic region, as well as the role of the n-type Schottky barrier. We show that reverse-bias operation eliminates complications caused by the n-type Schottky barrier and increases the length of the intrinsic region. The absorption cross-section of the CNT is calculated using an empirically verified model, and the effect of substrate reflection is determined using FDTD simulations. We find the room temperature photocurrent quantum yield is approximately 30% when exciting the carbon nanotube at the S_{44} and S_{55} excitonic transitions. The quantum yield value is an order of magnitude larger than previous estimates.

Keywords: Scanning Photocurrent, Microscopy, Excitons, Multiple Exciton Generation, Carrier Multiplication,

Nanomaterials are promising candidates for improving the performance of photodetectors and solar energy harvesting devices. Unique features of nanomaterials such as quantum confinement and strong electron-electron interactions can be harnessed to enhance the conversion of electromagnetic energy into electrical current. For example, the multiple exciton generation process in quantum dots has been used to boost the quantum efficiency of solar cell devices,^{1,2} and evidence of carrier multiplication (CM) has been observed in carbon nanotube (CNT) photodiodes.³

Carbon nanotubes are particularly promising because CM has been observed close to the energy conservation limit ($\hbar\omega = 2E_g$, where $\hbar\omega$ is photon energy and E_g is the CNT band gap).³ Experiments conducted at low-temperature ($T = 60$ K) on individual CNTs show that reverse-bias photocurrent increases dramatically when a CNT photodiode is illuminated with $\hbar\omega > 2E_g$ rather than $\hbar\omega < 2E_g$. While compelling, these experiments did not quantify the photocurrent quantum yield (QY), defined as the number of photogenerated carriers extracted from the device per absorbed photon. Robust methods of determining QY are needed to examine the physics of CM in CNTs.

One previous report has estimated the photocurrent QY of CNT photodiodes. Malapanis et al. measured individual CNT photodiodes in photovoltaic mode (no reverse bias) and found a room temperature photocurrent QY of 1 - 5%.⁴ The photodiodes used by Malapanis et al. were built from partially suspended CNTs with diameters in the range 1 – 2 nm. The whole device was illuminated, including the CNT-to-metal contacts. Photon energy was tuned to the first and second exciton transitions (S_{11} and S_{22}).

In this work, we study CNT pn junctions in a different regime. We use fully-suspended individual CNTs with diameters of 2 - 3 nm. The optical excitation energy is tuned to either S_{44} or

S_{55} and we study QY as a function of reverse bias. Using a focused laser spot we directly measure the length of the intrinsic region and isolate photocurrent from the pn junction. We find a photocurrent QY of 20 - 40%, an order of magnitude larger than previous work and a step closer to the ultimate goal of exceeding 100%.

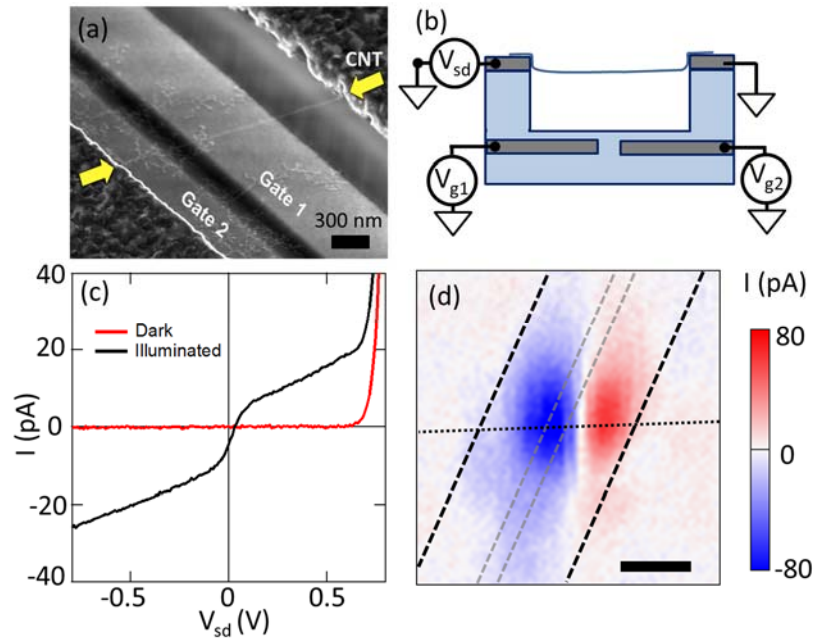


Figure 1. a) Scanning electron microscope image of the device geometry. b) Device schematic. c) Dark and illuminated diode curves from device 1 (red and black respectively). The illumination wavelength is 632nm and $V_{g2} = -V_{g1} = 8$ V. d) Scanning photocurrent microscopy image of device 1, $V_{g2} = -V_{g1} = 8$ V and $V_{sd} = 0$ V. The dotted line indicates the CNT axis. The black dashed lines indicate the source/drain electrode edges. The gray dashed lines indicate the split-gate electrode edges. The beam radius $a = 550$ nm. The scale bar is 1 μ m.

Our devices are made from single CNTs suspended above two split gates (Figure 1a,b). The distance between source and drain electrodes is 2 μ m and the separation between split gates is 250

nm. The top surface of the Pt source and drain electrodes is 770 nm above the top surface of the Pt split gates. A thin layer (~ 30 nm) of SiO₂ covers the split gates. The CNTs are grown as the last step of device fabrication. A fast-heat growth method is used to create pristine suspended CNTs free of chemical residue.⁵ We estimate the capacitance between each gate electrode and the suspended CNT to be approximately 4 aF/ μm (see Supporting Information). Fully-suspended CNTs grown in this way have been used to study a range of fundamental CNT properties.⁶

The suspended CNT diodes rectify current over a wide range of V_{sd} . The onset of reverse bias breakdown occurs when $|V_{\text{sd}}| > |V_{\text{g1}}|$. Under forward bias, an exponential increase in current, $I \propto \exp(eV_{\text{sd}}/nk_{\text{B}}T)$, is observed above a certain threshold voltage. Above this threshold we observe ideality factors, n , between 1.2 and 1.3 (see Supporting Information). Unlike a typical diode, the exponential current increase does not begin at $V_{\text{sd}} = 0$. The threshold for exponential current increase can be greater than 1 V (larger than E_{g}/e) in some gating configurations. This gate-tunable threshold shift was previously studied by Liu et al., who explained the behavior by analyzing the role of the n-type Schottky barrier.⁷ We have verified that our diodes exhibit the same gate-tunable I - V_{sd} behavior as reported in Ref. 7 (see Supporting Information).

Figure 1c shows the dark and illuminated diode curves of a device measured in air with $V_{\text{g2}} = -V_{\text{g1}} = 8$ V. The carrier concentration in the n-type and p-type regions is approximately $200 \mu\text{m}^{-1}$ (see Supporting Information). Illumination is performed with a defocused laser such that the CNT and metal electrodes are uniformly illuminated. The illuminated curve is strikingly different from a traditional photodiode. At negative bias, the photocurrent increases linearly with V_{sd} . At positive bias, between 0.1 – 0.6 V, the photocurrent also increases linearly with V_{sd} . The open circuit voltage, $V_{\text{oc}} \sim 50$ mV, is much lower than the band gap of a semiconducting CNT.

To understand the cause of these unusual characteristics, we performed scanning photocurrent microscopy (SPCM) using our home-built SPCM system.⁸ A focused laser spot is raster scanned over the surface while the reflected light and photocurrent are measured simultaneously. The laser spot has a Gaussian intensity profile, $\exp(-r^2/a^2)$ where r is the distance from the center of the beam and a is the beam radius. Figure 1d shows the scanning photocurrent microscopy (SPCM) image at $V_{sd} = 0$ with $a = 550$ nm. The negative photocurrent in the center of the CNT coincides with the expected position of the pn junction. The positive photocurrent near the right contact is close to the junction between the n-doped CNT and the metal electrode. The pattern in the photocurrent image (positive and negative spots elongated in the y-direction) is consistent with the superimposition of two Gaussian point spread functions of opposite sign centered 0.9 μm apart.

The zero-bias SPCM data suggests that there is a pn junction in the center of the suspended CNT and a Schottky diode where the n-type CNT meets the metal electrode. We tested this idea by repeating SPCM measurements at different values of V_{sd} . Figure 2 shows photocurrent profiles measured along the CNT axis. At $x = 0$ the laser is centered on the middle of the suspended CNT. At $x = \pm 1.1$ μm the laser is centered on the ends of the suspended CNT. When $V_{sd} > 0$, the photocurrent peak at $x = 0.9$ μm is enhanced. When $V_{sd} < 0$, the photocurrent peak at $x = 0$ is enhanced. When $V_{sd} = 0$, the two peaks are roughly equal.

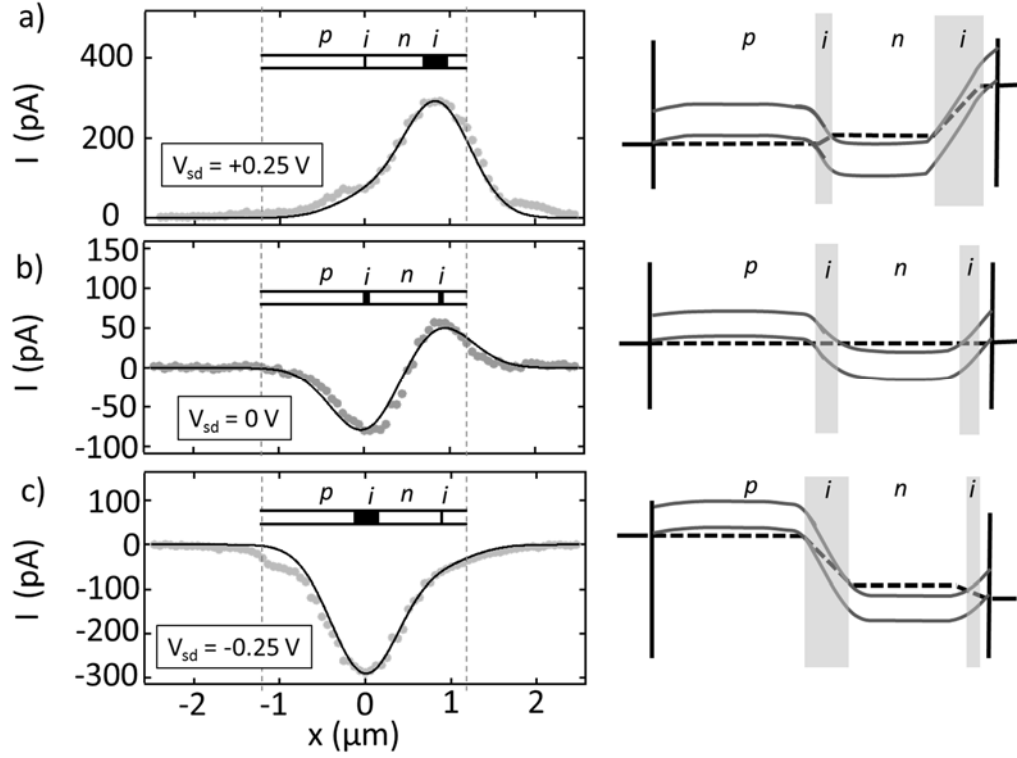


Figure 2. Photocurrent cross-sections (gray dots) measured along the CNT axis of device 1. The Gaussian beam radius is $a = 550$ nm. The laser is scanned with a step size of 60 nm. Solid black lines show fit curves constructed from Gaussian functions ($a = 550$ nm) centered at $x = 0$ and $x = 0.9$ μm . The bias voltages are a) $V_{sd} = +0.25$ V, b) $V_{sd} = 0$ V, and c) $V_{sd} = -0.25$ V.

The band bending diagrams accompanying Figure 2 illustrates our interpretation of the photocurrent peaks at $x = 0$ and 0.9 μm . When $V_{sd} = +0.25$ V, the peak centered at $x = 0.9$ μm dominates $I(x)$. The n-type Schottky barrier is in reverse bias, which increases the length of the intrinsic region near the contact, L_{Sch} . Assuming $L_{\text{Sch}} < a$, we expect a peak photocurrent

$$I_{\text{Sch}}^{\text{PC}} \approx +e\eta\Phi_0\sigma_c N' L_{\text{Sch}},$$

where η is the photocurrent QY, Φ_0 is the photon flux at the center of the laser spot, σ_c is the absorption cross section per carbon atom and N' is the number of carbon atoms per unit length. The sign of the current is determined by the direction of the local electric field. When $V_{sd} = -0.25$ V, the peak centered at $x = 0$ dominates. The pn junction is in reverse bias which increases the length of the intrinsic region in the center of the CNT, L . Assuming $L < a$, we expect a peak photocurrent

$$I_{pn}^{PC} \approx -e\eta\Phi_0\sigma_c N' L$$

In summary, I_{Sch}^{PC} and I_{pn}^{PC} have opposite sign due to the opposing local electric fields. I_{Sch}^{PC} grows when $V_{sd} > 0$ because L_{Sch} increases. I_{pn}^{PC} grows when $V_{sd} < 0$ because L increases. Near $V_{sd} = 0$, I_{pn}^{PC} and I_{Sch}^{PC} become equal and opposite.

The model depicted in Fig. 2 helps explain the illuminated diode curve shown in Fig 1c. The illuminated diode curve is measured using a defocused laser (uniform Φ_0 across the whole device), therefore the net photocurrent is $I_{pn}^{PC}(V_{sd}) + I_{Sch}^{PC}(V_{sd})$. Adding these opposing photocurrents results in three distinct segments of the illuminated I - V_{sd} curve. At negative V_{sd} , the net photocurrent is dominated by I_{pn}^{PC} . At positive V_{sd} , the net photocurrent is dominated by I_{Sch}^{PC} . When V_{sd} is close to zero, the two photocurrents cancel each other. These three V_{sd} regimes appear as three different slopes in Fig 1c.

In the context of photocurrent QY measurements, the key insight is that I_{pn}^{PC} dominates when $V_{sd} < 0$. The disappearance of I_{Sch}^{PC} indicates a flat band condition where the n-type CNT meets the electrode. We conclude that a small negative V_{sd} is ideal for studying the photocurrent generation process in the suspended CNT pn junction. Reverse bias is used for this purpose throughout the rest of this paper.

Our goal is to determine the photocurrent QY from the pn junction. As a working model, we assume the photocurrent QY has a constant value, η , within the intrinsic region of the pn junction. We assume that QY is zero everywhere else because Auger processes lead to extremely short minority carrier lifetimes in doped CNTs.^{9,10} If photocurrent is excited by a Gaussian laser spot with photon flux $\Phi(r) = \Phi_0 \exp(-r^2/a^2)$, we expect peak photocurrent

$$I_{\text{peak}} = -e\eta\Phi_0\sigma_c N' a \sqrt{\pi} \operatorname{erf}\left(\frac{L}{2a}\right) \quad (1)$$

We determine I_{peak} and a from SPCM imaging. Determination of the other variables, $\sigma_c N'$, Φ_0 , and L is discussed below.

Systematic determination of $\sigma_c(\hbar\omega)$ has recently has been accomplished,^{11,12} allowing us to calculate $\sigma_c N'$ based on the chiral index of the CNT. We determine the chiral index by measuring the photocurrent spectra (Figure 3a). The light source for this measurement is a supercontinuum laser (Fianium SC450 with 40 MHz repetition rate) filtered by a double-monochromator in subtractive mode. The light is defocused ($a \sim 10 \mu\text{m}$) and polarized parallel to the CNT axis. The peaks in the photocurrent spectrum are compared to the CNT atlas,¹³ as detailed in our previously published method.¹⁴ After identifying the chiral index that matches the observed exciton resonances, $\sigma_c(\hbar\omega)$ is calculated using empirically verified expressions for oscillator strength and linewidth of the exciton and continuum transitions.¹¹ The predicted absorption spectrum for Device 1 (parallel polarization) is plotted in Figure 3b. The energy-averaged σ_c (horizontal dashed line) is approximately equal to the absorption cross-section of graphene, as expected from the f-sum rule.

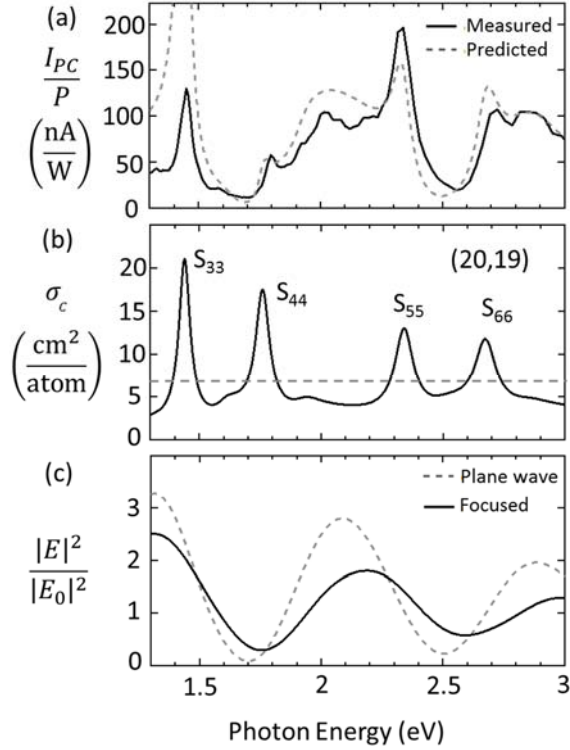


Figure 3. a) Photocurrent spectrum measured from device 1 (solid line). Calculated photocurrent spectra based on absorption cross section and intensity enhancement factor (dashed line). b) Calculated (solid line) and energy-averaged (dashed line) absorption cross section. c) Calculated intensity enhancement factor for focused beam (solid line) and plane wave (dashed line).

The photon flux, Φ , includes contributions from both incident and reflected light, and is complicated by interference effects. To determine Φ , we performed FDTD simulations with LumericalTM software. Our simulations calculate the wavelength-dependent intensity-

enhancement factor $\frac{|E|^2}{|E_0|^2}$, where E and E_0 are optical electric fields determined at the CNT position when the device structure is respectively present or absent. We have performed simulations for both a defocused and focused laser (Figure 3c). The defocused beam is relevant for understanding the photocurrent spectrum (Figure 3a), while the focused beam is used to interpret the SPCM measurements. The calculated intensity enhancement factor accurately predicts the suppression of photocurrent at photon energies near 1.8 eV and 2.6 eV (Figure 3a) if we assume the CNT is 675nm above the reflecting surface of the split-gate electrodes. Comparing $\frac{|E|^2}{|E_0|^2} \cdot \sigma_c(\hbar\omega)$ (dashed line in Figure 3a) to the measured photocurrent spectrum reveals excellent agreement in the energy range 1.5 – 3 eV, giving us confidence in our understanding of the intensity enhancement factor. The discrepancy at low photon energy is suggestive of reduced η . The energy dependence of η is discussed further below.

To determine the length of the intrinsic region, L , we maximize the spatial resolution of our SPCM by reducing the beam radius (100X objective, NA = 0.8). The measurements are performed in a vacuum environment to minimize gate hysteresis effects. Interestingly, the vacuum environment has an additional effect of reducing the photocurrent generated at the n-type Schottky barrier when the device is operated at $V_{sd} = 0$. The reduced effect of the Schottky barrier is likely due to a change in Fermi-level pinning.¹⁵ Figure 4a shows an image obtained with $V_{sd} = -0.5$ V and $a = 0.37$ μm . The photocurrent spot is symmetric and corresponds to the point spread function of the laser. The faint halo around the main photocurrent spot is caused by the Airy disk pattern generated by overfilling the back plane of the objective. When the reverse bias is increased, the photocurrent spot elongates along the CNT axis, suggesting an increase in L . We quantify L by comparing the photocurrent profile, $I(x)$, to the expected profile from an intrinsic region of length L ,

$$I(x) = e\eta\Phi_0\sigma_c N'a \frac{\sqrt{\pi}}{2} \left[\operatorname{erf}\left(\frac{x - \frac{L}{2}}{a}\right) - \operatorname{erf}\left(\frac{x + \frac{L}{2}}{a}\right) \right]. \quad (2)$$

Equation 2 reduces to eq 1 when $x = 0$. Figure 4c shows the measured photocurrent profiles, together with the fit curves.

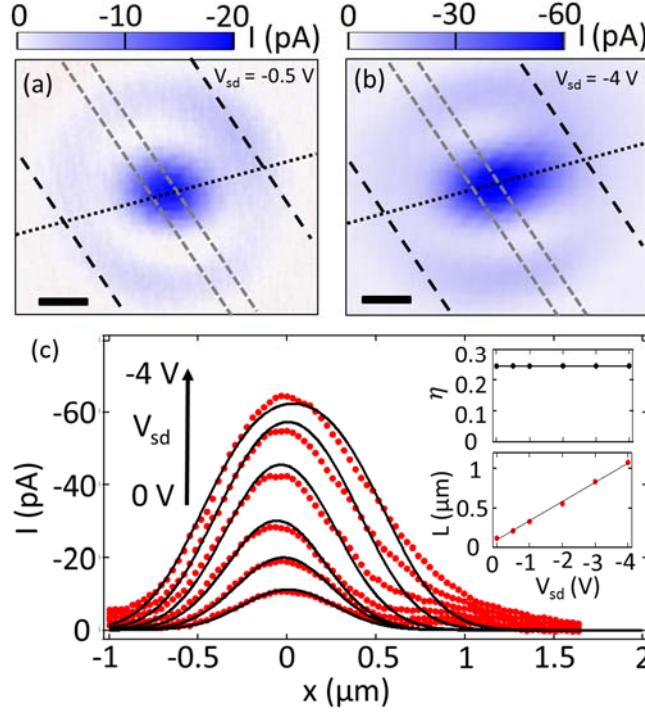


Figure 4. a-b) High resolution photocurrent images of device 3 (100X objective with NA 0.8), $a = 0.37 \mu\text{m}$, $V_{g2} = -V_{g1} = 10 \text{ V}$, $P_{\text{laser}} = 1.56 \mu\text{W}$, and $\hbar\omega = 2.54 \text{ eV}$ a) $V_{\text{sd}} = -0.5 \text{ V}$, b) $V_{\text{sd}} = -4 \text{ V}$. Scale bars are $1 \mu\text{m}$. c) Photocurrent cross-sections at $V_{\text{sd}} = 0, -0.5, -1, -2, -3,$ and -4 V (red dots). Fitted curves using eq 2. Inset: Curve fitting parameters.

We obtain good fits to the SPCM cross sections by assuming η is independent of V_{sd} and adjusting L for each curve. The resulting values of η and L are shown in the inset of Figure 4c. There are other approaches to fitting the data, for example, leaving both η and L as free parameters when $L > 0.37 \mu\text{m}$. These alternative fitting procedures lead to qualitatively similar results.

The constant η hypothesis results in a near perfect linear relationship between L and V_{sd} (see inset Fig. 4c). This linear relationship between L and V_{sd} is consistent with the illuminated diode curve (Fig. 1c) and can be explained using a simple electrostatic model. The integral of the electric field across the pn junction depends on V_{sd} and E_g ,

$$\int \mathcal{E}(x)dx = \alpha V_{sd} - E_g/e,$$

where $\mathcal{E}(x)$ is the component of electric field pointing along the CNT axis, and α is the fraction of V_{sd} that drops across the pn junction. The magnitude of $\int \mathcal{E}(x)dx$ grows when V_{sd} becomes more negative. The integral is approximately equal to the product $\mathcal{E}_{\max}L$, where \mathcal{E}_{\max} is the maximum value of $\mathcal{E}(x)$. \mathcal{E}_{\max} depends strongly on V_{g1} , V_{g2} and the charge density profile along the CNT, but has relatively weak dependence on V_{sd} (there is no appreciable change in the charge density profile when $|V_{sd}| \ll |V_{g1,g2}|$). Therefore, we expect the linear relationship between $\mathcal{E}_{\max}L$ and V_{sd} to be driven by L , while \mathcal{E}_{\max} stays constant. Based on the experimentally determined relationship between L and V_{sd} (inset of Fig. 4) we estimate $\mathcal{E}_{\max} \approx -4 \text{ V}/\mu\text{m}$ for the gate voltages used here. A similar electric field strength was recently calculated by solving Poisson's equation iteratively to find a self-consistent charge density profile in a suspended CNT device with $V_{g2} = -V_{g1} = 9 \text{ V}$.¹⁶

After establishing robust methods to determine $\sigma_c N'$, Φ_0 , and L , we measured η in three devices (Table 1). The supercontinuum light source was polarized parallel to the CNT axis and tuned to an exciton resonance (either S_{44} or S_{55}). The intensity was reduced below $1 \text{ kW}/\text{cm}^2$ to ensure that measurements are performed in the linear regime. At higher laser powers we have observed sub-linear power dependence, as reported by other authors.¹⁷ A reverse bias $V_{sd} = -4\text{V}$ was used to make L and I_{peak} more experimentally accessible.

Device	(n, m)	D (nm)	E_g (eV)	$\hbar\omega = S_{xx}$	$\sigma_c N'$ (nm)	Power (μW)	$\frac{ E ^2}{ E_0 ^2}$	a (μm)	L (μm)	I_{peak} (pA)	η
1	(20, 19)	2.65	0.53	2.34 eV = S_{55}	0.402	4.21	1.42	0.48	1.25	415	0.39
2	(22, 9)	2.17	0.63	2.13 eV = S_{44}	0.436	3.29	1.65	0.55	1.64	241	0.21
3	(18, 17)	2.37	0.59	1.92 eV = S_{44}	0.495	3.19	0.61	0.58	1.07	134	0.27
3	(18, 17)	2.37	0.59	2.54 eV = S_{55}	0.367	2.51	0.78	0.42	1.07	138	0.42

Table 1. Determination of photocurrent QY, η , when $\hbar\omega = S_{44}$ or S_{55} . I_{peak} was measured with a 50X objective (NA = 0.5) and $V_{\text{sd}} = -4$ V, $V_{\text{g2}} = -V_{\text{g1}} = 10$ V. η is calculated using eq 1. CNT band gap is estimated using $E_g = S_{11} + X_b$, where $X_b \approx 340$ meV \cdot nm/ D is the exciton binding energy in the first sub band.¹⁸

We find that η is approximately 0.3 for the conditions we have studied. This result has implications for understanding the energy relaxation pathways in CNTs. The relaxation process is expected to occur on the femtosecond timescale,¹⁹ three orders of magnitude faster than the escape time from the pn junction.¹⁷ The photoexcited S_{44} (or S_{55}) excitons will decay into low energy excitons (S_{11}) and free carriers in the first sub-band ($e_1 + h_1$). Theoretical work predicts that S_{11} production is strongly favored over $e_1 + h_1$ production.²⁰ While transient absorption spectroscopy experiments at room temperature show that multiple S_{11} excitons can be created from a single photon,²¹ only a fraction of S_{11} excitons will be dissociated by \mathcal{E} and contribute photocurrent.²² An additional mechanism for CM in CNTs is impact ionization by free carriers that are accelerated by \mathcal{E} .³ However, impact ionization is not expected to persist at room temperature due to phonon friction.²³ In summary, we speculate that our experiment generates a large

population of S_{11} excitons, but a smaller population of $e_1 + h_1$ which results in a photocurrent QY less than 1.

Table 1 shows a trend toward higher η at higher photon energy. For S_{44} excitation, the average η is 0.24. For S_{55} excitation the average η is 0.41. An increase in η with $\hbar\omega$ is consistent with CM mechanisms, i.e. excess photon energy $\hbar\omega - E_g$ is directed into increased carrier generation.

The increase in η at higher excitation energies may partially explain our higher QY values compared to earlier measurements by Malapanis et al. (these previous measurements used S_{11} and S_{22} excitation).⁴ Additional differences that may contribute to our higher QY values include larger diameter CNTs (exciton binding energy $\sim 1/D$) and our experimental method that directly measures L and mitigates the effect of I_{Sch}^{PC} .

In conclusion, we have developed a robust method to determine photocurrent QY from individual CNT pn junctions. We observe photocurrent QY values in the range 20 - 40% in suspended CNT pn junctions measured at room temperature with built-in electric field ≈ 4 V/ μ m. It is likely that multiple S_{11} excitons are also generated during the photoexcitation process, but are not registered in our photocurrent measurement. Enhancement of photocurrent QY from impact ionization processes is likely suppressed at room temperature. Our results set a new benchmark for the performance of CNT pn junctions in photodetector and energy harvesting applications. Promising directions for future work include increasing electric field strength, decreasing temperature, and modifying the dielectric environment to reduce exciton binding.²⁴ With optimized conditions, CNTs show promise for achieving photocurrent QY greater than unity.

ASSOCIATED CONTENT

Supporting Information

Field-effect transistor measurements of a split-gate suspended CNT device. Diode curves ($\log(I)$ vs. V_{sd}) for a suspended CNT pn junction with various V_{g1} and V_{g2} . Additional discussion of the diode characteristics. Measurement of gate capacitance. This material is available free of charge via the Internet at <http://pubs.acs.org>.

AUTHOR INFORMATION

Corresponding Author

*Email: ethan.minot@oregonstate.edu

Note: The authors declare no competing financial interest.

ACKNOWLEDGMENTS

This material is based upon work supported by the National Science Foundation under Grant No. 1151369. A portion of device fabrication was carried out in the University of California Santa Barbara (UCSB) nanofabrication facility. We thank Gary Steele and Joshua Island for assistance with gate capacitance measurements (Fig S3) and Morgan Brown for scanning electron microscope images (Fig 1a).

REFERENCES

- (1) Semonin, O. E.; Luther, J. M.; Choi, S.; Chen, H.-Y.; Gao, J.; Nozik, A. J.; Beard, M. C. *Science* **2011**, *334* (6062), 1530–1533.
- (2) Sambur, J. B.; Novet, T.; Parkinson, B. A. *Science* **2010**, *330*, 63–66.
- (3) Gabor, N. M.; Zhong, Z.; Bosnick, K.; Park, J.; McEuen, P. L. *Science* (80-.). **2009**, *325*

- (5946), 1367–1371.
- (4) Malapanis, A.; Perebeinos, V.; Comfort, E.; Sinha, D. P.; Lee, J. U.; Comfort, E.; Lee, J. U. *Nano Lett.* **2013**, *13* (8), 3531–3538.
 - (5) Cao, J.; Wang, Q.; Rolandi, M.; Dai, H. *Phys. Rev. Lett.* **2004**, *93* (21), 216803.
 - (6) Laird, E. A.; Kuemmeth, F.; Steele, G. A.; Grove-Rasmussen, K.; Nygård, J.; Flensberg, K.; Kouwenhoven, L. P. *Rev. Mod. Phys.* **2015**, *87* (3), 703–764.
 - (7) Liu, C. H.; Wu, C. C.; Zhong, Z. *Nano Lett.* **2011**, *11* (4), 1782–1785.
 - (8) DeBorde, T.; Kevek, J. W.; Sharf, T.; Wardini, J. L.; Minot, E. D. *Proc. IEEE Conf. Nanotechnol.* **2011**, 382–386.
 - (9) Wang, F.; Dukovic, G.; Knoesel, E.; Brus, L. E.; Heinz, T. F. *Phys. Rev. B* **2004**, *70* (24), 241403.
 - (10) Yasukochi, S.; Murai, T.; Moritsubo, S.; Shimada, T.; Chiashi, S.; Maruyama, S.; Kato, Y. K. *Phys. Rev. B* **2011**, *84* (12), 121409.
 - (11) Liu, K.; Hong, X.; Choi, S.; Jin, C.; Capaz, R. B.; Kim, J.; Wang, W.; Bai, X.; Louie, S. G.; Wang, E.; Wang, F. *Proc. Natl. Acad. Sci. U. S. A.* **2014**, *111* (21), 7564–7569.
 - (12) Blancon, J.-C.; Paillet, M.; Tran, H. N.; Than, X. T.; Guebrou, S. A.; Ayari, A.; San Miguel, A.; Phan, N.-M.; Zahab, A.-A.; Sauvajol, J.-L.; Del Fatti, N.; Vallée, F. *Nat. Commun.* **2013**, *4*, 2542.
 - (13) Liu, K.; Deslippe, J.; Xiao, F.; Capaz, R. B.; Hong, X.; Aloni, S.; Zettl, A.; Wang, W.; Bai, X.; Louie, S. G.; Wang, E.; Wang, F. *Nat. Nanotechnol.* **2012**, *7* (5), 325–329.

- (14) Deborde, T.; Aspitarte, L.; Sharf, T.; Kevek, J. W.; Minot, E. D. *J. Phys. Chem. C* **2014**, *118* (19), 9946–9950.
- (15) Derycke, V.; Martel, R.; Appenzeller, J.; Avouris, P. *Appl. Phys. Lett.* **2002**, *80* (15), 2773–2775.
- (16) Chang, S. W.; Hazra, J.; Amer, M.; Kapadia, R.; Cronin, S. B. *ACS Nano* **2015**, *9* (12), 11551–11556.
- (17) Gabor, N.; Zhong, Z.; Bosnick, K.; McEuen, P. *Phys. Rev. Lett.* **2012**, *108* (8), 087404.
- (18) Dukovic, G.; Wang, F.; Song, D.; Sfeir, M. Y.; Heinz, T. F.; Brus, L. E. *Nano Lett.* **2005**, *5* (11), 2314–2318.
- (19) Perebeinos, V.; Avouris, P. *Phys. Rev. B* **2006**, *10598* (1), 1–5.
- (20) Hertel, T.; Perebeinos, V.; Crochet, J.; Arnold, K.; Kappes, M.; Avouris, P. *Nano Lett.* **2008**, *8* (1), 87–91.
- (21) Wang, S.; Khafizov, M.; Tu, X.; Zheng, M.; Krauss, T. D. *Nano Lett.* **2010**, *10* (7), 2381–2386.
- (22) Chang, S.-W.; Theiss, J.; Hazra, J.; Aykol, M.; Kapadia, R.; Cronin, S. B. *Appl. Phys. Lett.* **2015**, *107* (5), 053107.
- (23) Baer, R.; Rabani, E. *Nano Lett.* **2010**, *10* (9), 3277–3282.
- (24) Perebeinos, V.; Tersoff, J.; Avouris, P. *Phys. Rev. Lett.* **2004**, *92* (25 I), 257402–1.

